# REPORT DOCUMENTATION PAGE

| 1. REPORT DATE (DD-MM-YYYY) | 2. REPORT TYPE | 3. DATES COVERED (From - To) |
|---|---|---|
| 09-28-2008 | Final | 15 April 2007 to 30 May 2008 |

**4. TITLE AND SUBTITLE**

Continuing Experiments on the Receptivity of Transient Disturbances to Surface Roughness and Freestream Turbulence

**5a. CONTRACT NUMBER**

**5b. GRANT NUMBER**
FA9550-07-1-0312

**5c. PROGRAM ELEMENT NUMBER**

**6. AUTHOR(S)**
Edward B. White

**5d. PROJECT NUMBER**

**5e. TASK NUMBER**

**5f. WORK UNIT NUMBER**

**7. PERFORMING ORGANIZATION NAME(S) AND ADDRESS(ES)**

Texas Engineering Experiment Station
200 Greens Prairie Road
College Station, TX 77845

**8. PERFORMING ORGANIZATION REPORT NUMBER**

**9. SPONSORING/MONITORING AGENCY NAME(S) AND ADDRESS(ES)**

Air Force Office of Scientific Research
875 North Randolph Street
Arlington, Va., 22203

**10. SPONSOR/MONITOR'S ACRONYM(S)**

**11. SPONSOR/MONITOR'S REPORT NUMBER(S)**
AFRL-OSR-VA-TR-2012-0562

**12. DISTRIBUTION/AVAILABILITY STATEMENT**

A Distribution Statement A: Approved for public release. Distribution is unlimited

**13. SUPPLEMENTARY NOTES**

**14. ABSTRACT**

Transient growth is a boundary-layer instability mechanism that leads to algebraic growth of disturbances generated by surface roughness. Earlier research programs verified that roughness-induced transient disturbances are not optimal and depend critically on the details of the receptivity process. This project seeks to provide a more complete understanding of the receptivity of transient disturbances to a spanwise array of cylindrical roughness elements using biorthogonal decomposition. Both experimental and direct numerical simulation (DNS) data sets are used as inputs to the decomposition procedure. The DNS data is successfully decomposed and provides accurate predictions of downstream disturbance growth. The experimental data is not sufficiently accurate to provide successful decomposition. For this, it appears that at least the spanwise disturbance components must be measured with better accuracy than was achieved in this project. Work will continue on this topic because DNS cannot presently model surfaces with realistic distributed roughness.

**15. SUBJECT TERMS**

transient growth, boundary-layer instability, boundary-layer transition, laminar-turbulent transition, roughness, receptivity, adjoint

| 16. SECURITY CLASSIFICATION OF: | | | 17. LIMITATION OF ABSTRACT | 18. NUMBER OF PAGES | 19a. NAME OF RESPONSIBLE PERSON |
|---|---|---|---|---|---|
| a. REPORT | b. ABSTRACT | c. THIS PAGE | | 28 | |
| | | | | | 19b. TELEPHONE NUMBER (Include area code) |

# Final Report for AFOSR Grant FA9550-07-1-0312

# Continuing Experiments on the Receptivity of Transient Disturbances to Surface Roughness and Freestream Turbulence

**Edward B. White**
Department of Aerospace Engineering
Texas A&M University
College Station, TX 77843-3141

## Summary

Transient growth is a boundary-layer instability mechanism that leads to algebraic growth of disturbances generated by surface roughness and freestream turbulence. Earlier AFOSR-funded research programs verified that stationary, roughness-induced disturbances undergo transient growth but that these disturbances are not optimal and depend critically on the details of the receptivity process. This project seeks to provide a more complete understanding of the receptivity of transient disturbances to surface roughness through a rigorous decomposition of steady disturbances across the continuous spectrum of Orr–Sommerfeld/Squire (OS) eigenmodes. This is achieved using the biorthogonal system of adjoint OS eigenmodes following an approach developed by Tumin (2003). Steady disturbances are generated using a spanwise array of cylindrical roughness elements and are measured using hotwire anemometry. Data resulting from an independent direct numerical simulation (DNS) of the experiment is also used as inputs to the biorthogonal decomposition.

Biorthogonal decomposition of the DNS data was successful. Disturbance profiles are reproduced with good accuracy and disturbance evolution is predicted with good accuracy for a distance exceeding 100 boundary-layer scales downstream of the decomposition location. These results represent the first rigorous quantification of transient growth receptivity to realizable disturbance inputs in boundary layers. They are also the first to quantitatively describe the way in which realizable disturbance differ from optimal disturbances.

Similar decomposition efforts using the experimental data as input was not successful. It appears that the spanwise disturbance components of the measurements hinder accurate decomposition. But, when they are not included in the partial data input to the decomposition, there is insufficient information to predict downstream behavior. A Monte Carlo–based technique was developed to provide a thorough examination of the experimental uncertainties of the spanwise disturbance data. This approach provided good information about the uncertainties but did not reveal the source of the spanwise disturbance measurement errors. Work will continue toward successful decomposition of experimental data because DNS of realistic surfaces remains prohibitively costly.

The project involved one faculty member and two graduate students and two undergraduate students at Texas A&M University. The project P.I. was Edward B. White, an associate professor in the Department of Aerospace Engineering. The two graduate students were Robert S. Downs III and Nicholas. A. Denissen. Both are Ph.D. candidates in Aerospace Engineering.

i

# Contents

# Final Report for AFOSR Grant FA9550-07-1-0312

# Continuing Experiments on the Receptivity of Transient Disturbances to Surface Roughness and Freestream Turbulence

**Edward B. White**
Department of Aerospace Engineering
Texas A&M University
College Station, TX, 77843-3141

## 1    Introduction and Objectives

### 1.1    Background

The stability of boundary layers has been analyzed most successfully using a normal mode decomposition of the Navier–Stokes equations linearized about a steady basic state. Using this approach, a flow is considered unstable if any of its disturbance modes are subject to exponential growth or stable if all of its modes are subject to exponential decay. This analysis leads to the familiar Orr–Sommerfeld/Squire (OS) equations that can be solved using either a temporal or spatial formulation. The solution describes the growth and decay of Tollmien–Schlichting (TS) waves at various Reynolds numbers, wave numbers and frequencies. For 2-D boundary layers, Squire's Theorem gives the well-known result that 2-D, streamwise-traveling disturbances (i.e., those with spanwise wavenumber $\beta = 0$) are destabilized at lower Reynolds numbers than obliques waves and, consequentially, most of the work done to date on this system has focused on the growth of 2-D waves because they have been viewed as the most important to the transition process.

While this approach successfully describes the boundary layer when the initial disturbance amplitudes are very low, a number of important problems that include high-amplitude freestream turbulence, high-amplitude surface roughness, or both, undergo a transition process that includes disturbance growth in regions where the Reynolds number is small and all the normal modes are subject to exponential decay. This phenomenon was named *bypass transition* because the disturbances were said to bypass the well-understood TS route to turbulence. For many years bypass was attributed to unknown nonlinear interactions of the disturbance modes, not because of any direct evidence of such interactions, but rather because the transition mechanism in those cases defied any other explanation (Reshotko 2001).

A relatively recent development that addresses the bypass transition question is a theory known as *transient growth*. Transient growth is an attractive theory because it appears to be capable of explaining many subcritical (i.e., subcritical to the growth of TS waves) transition phenomena of heretofore unknown origin, especially those involving spanwise-varying disturbances, exactly the sort of disturbances produced by surface roughness or freestream turbulence. Transient growth is fundamentally different than TS wave growth because it results from an *inviscid* rather than a viscous mechanism and produces *algebraic* rather than exponential growth. Disturbances that experience this algebraic transient growth eventually decay exponentially but, prior to this decay, they are capable of undergoing very significant growth and should therefore be considered to be equally likely as TS waves to lead to transition. Despite the original suspicion to the contrary, transient growth is a linear mechanism.

1

In order to quantify how much disturbance growth might result from transient growth, Farrell (1988) introduced the concept of an optimal disturbance. Farrell examined the initial value problem in an optimization context to find the initial disturbance that produces the maximum disturbance kinetic energy at a specified later time. Studies by Butler and Farrell (1992) and later studies by Andersson et al. (1999), Luchini (2000) and Tumin and Reshotko (2001) have identified that the optimal disturbances in Blasius boundary layer are stationary ($\omega = 0$), streamwise-oriented vortices that evolve into streamwise streaks. The spanwise wavenumber for the optimal disturbance is $\beta = 0.45$ where $\beta$ is made dimensionless using the boundary-layer scale, $\delta$.

Prior to a previous AFOSR Project (FA9620-02-1-0058), no experiments had been performed to deliberately examine whether transient growth of stationary disturbances occurs or whether roughness generates transient disturbances. Some evidence suggested that roughness can lead to transient growth (Tani et al. 1962; Reshotko and Leventhal 1981; Kendall 1981) but none of relevant experiments were conducted in a way that could conclusively verify this idea. Experiments conducted as part of AFOSR Project FA9620-02-1-0058 conclusively established that roughness does indeed stationary transient disturbances. But, those disturbances do not behave as optimal disturbance theory predicts.

A more recent AFOSR-funded project, FA9550-05-1-0048, continued to study transient growth with a specific emphasis on *receptivity*. The original intent of that project was (1) to explore means of quantifying the receptivity of regular arrays of surface roughness, (2) to investigate distributed receptivity that occurs over randomly distributed three-dimensional surface roughness, and (3) to investigate receptivity to freestream turbulence. These three objectives were to be completed over a three-year period at Case Western Reserve University (CWRU). However, the project was canceled after two years when the PI, Prof. Edward White, moved from CWRU to Texas A&M University (TAMU). During the first two years of the project the second objective (investigating receptivity to distributed roughness) was completed and much of the work of first objective (quantifying receptivity) was completed. The present report details the one-year follow-on effort at TAMU to complete the first objective. The third objective (investigating receptivity to freestream turbulence), was not pursued due to delays with facility construction.

## 1.2  Results of previous AFOSR-funded experiments

As described above, experiments conducted as part of AFOSR Project FA9620-02-1-0058 were the first to deliberately examine whether surface roughness produces transient disturbances. Those experiments were conducted using cylindrical roughness elements arranged in a spanwise-oriented array some distance downstream of the leading edge of a flat plate, $x_k$. The plate was oriented to provide a low-speed, zero-pressure-gradient Blasius boundary layer. The roughness heights, $k$, and spanwise spacings, $\lambda_k$, were systematically varied to determine the effects of these parameters on the resulting disturbances. Also varied was the ratio between the roughness elements' diameters, $D$, and the roughness elements' spanwise spacing. A sketch of the experimental setup is shown in Fig. 1.

A number of key findings resulted from the experiments. These are principally reported by White (2002), White et al. (2005) and Ergin and White (2006). First, White (2002) establishes that spanwise arrays of 3D roughness elements do indeed generate stationary disturbances that undergo transient growth. White (2002) links the discrepancy between the theoretical predictions for optimal disturbances and the experimental observation to receptivity. That is, the process by which the roughness generates an initial disturbance distributes energy across the continuous OS spectrum in a way that differs from the optimum distribution.

In order to better understand receptivity issues, White et al. (2005) conducted detailed studies
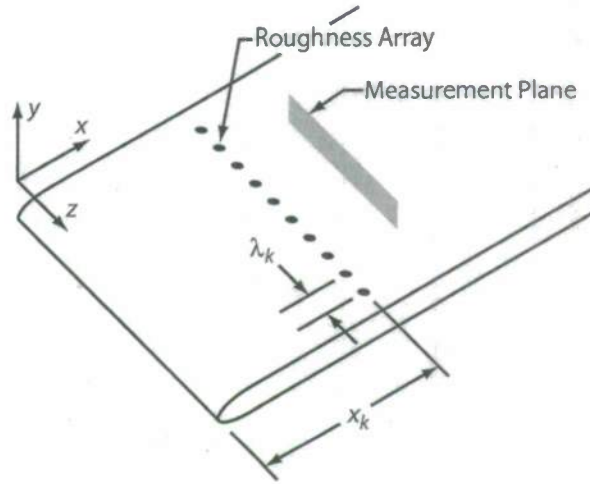
Figure 1: Coordinate system, roughness array parameters and measurement plane orientation.

that varied $Re_k$ and $D/\lambda_k$ for a roughness array at a fixed $x_k$ and unit Reynolds number, $Re' = U_\infty/\nu$. The experiments focused on the role of $Re_k$ varied this parameter between values of 16 and 195 while maintaining $D/\lambda_k = 1/3$. For this configuration, certain spanwise modes undergo clear transient growth, the modes whose wavelengths are $\lambda_k/3$ and $\lambda_k/4$, in particular. However, the $\lambda_k$ mode shows only weak growth after a dramatic initial decay; the $\lambda_k/2$ mode only decays. Again, the key conclusion is that the distribution of initial disturbance energy amongst the relevant continuous modes is critical to the nature and magnitude of the transient growth. Moreover, no realizable disturbance appears to be optimal. While the experiments revealed that realizable disturbances are not optimal in a qualitative sense, it was not possible at that time to quantify the way in which realizable disturbances differ from optimal disturbances.

The data presented by White et al. (2005) only extend to $Re_k = 195$ because beyond that value, bypass transition occurs; Rice (2004) observed bypass at $Re_k = 254$ for the same configuration. To examine the nature of this bypass transition, Ergin and White (2006) extended the $Re_k$ range to $Re_k = 339$ and made a detailed study of the steady and unsteady flow at subcritical and this supercritical $Re_k$. Those experiments revealed unsteady $u'$ fluctuations in the roughness elements' wakes that grow while the $U'$ disturbance is large. The most significant growth is associated with regions of large $\partial U'/\partial z$ gradients. The $u'$ growth is exponential and is thus thought to be the result of a Kelvin–Helmholtz-type instability; it is not transient growth of unsteady disturbances. Once the $U'$ disturbance has sufficiently decayed, the $u'$ disturbances decay as well. At $Re_k = 202$ and 264, the initial $U'$ disturbance is sufficiently small that the flow becomes stable to growing $u'$ disturbances before they grow to large amplitude. However, in the supercritical case, the $u'$ amplification rates are higher and persist for a longer streamwise distance. This gives the unsteady disturbances the ability to grow and bring about transition before they stabilize.

After the bypass experiments by Ergin and White (2006) were completed, a DNS of the setup was performed by Rizzetta and Visbal (2007) for $Re_k$ values of 202 and 339. Those computations confirmed the basic transition mechanism identified by Ergin and White. However, the DNS found that for the supercritical case, $Re_k = 339$, transition occurs much farther downstream in the experiment than it does in the computation. Also, the computation shows significantly more fine-scale disturbance detail than does the experiment. Thus, there was some concern that the $Re_k$ values reported by Ergin and White (2006) might have been incorrect. If the reported values were lower than the actual values,
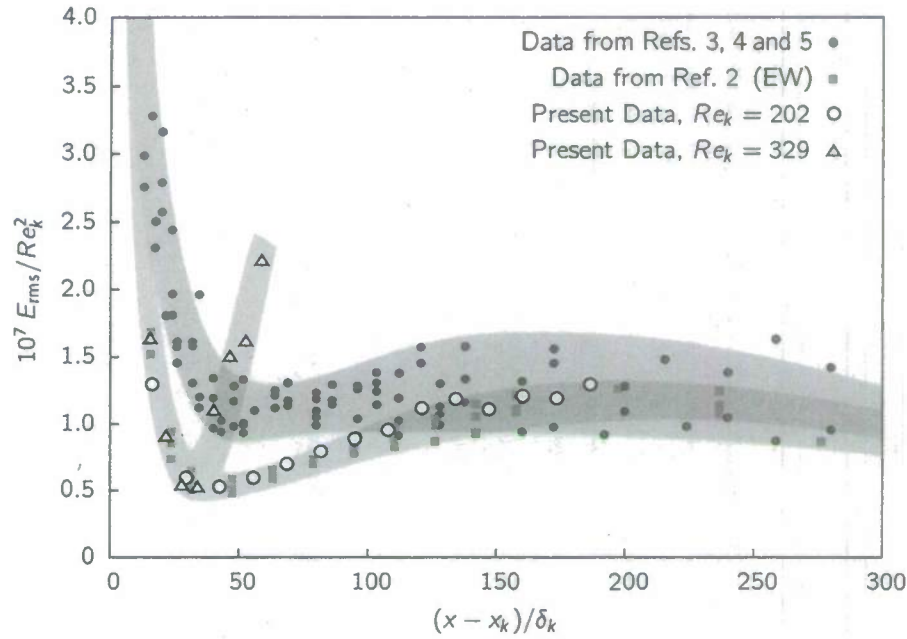
Figure 2: Scaled disturbance energies.

this would result in the discrepancies between the DNS and experimental results.

To resolve the inconsistencies between the experiments by Ergin and White (2006) and the DNS by Rizzetta and Visbal (2007), an experiment was conducted by Denissen and White (2008) that duplicated the dimensionless parameters of the Ergin and White experiment. The results of this new experiment suggests the previous experiment and the DNS are largely in agreement. The results also revealed that the Reynolds number based on the boundary-layer thickness at the roughness location, $Re_{\delta_k}$, has a more significant effect on transient growth than previously believed. A principal difference between the Ergin and White results and the more-recent Denissen and White results is that Denissen and White observe the small-scale features present in the DNS while the earlier experiment did not. This might be attributable to the somewhat wider element-to-element spacing used by Denissen and White and/or the fact that their experiment used sharp-edged manufactured roughness elements while the earlier experiment used paper elements. Denissen and White also confirm the DNS prediction for breakdown location. The longer breakdown distance in the Ergin and White experiment is attributable to nonuniformities in the paper roughness elements. Finally, the new result by Denissen and White is a clarification of the role of $Re_{\delta_k}$. Figure 2 shows the stationary disturbance energies measured by White and Ergin (2003), Rice (2004) and White et al. (2005) (blue symbols) plus those by Ergin and White (2006) and Denissen and White (2008) (red symbols). This figure shows two clear bands of total disturbance energy that are consistent across large ranges of $Re_k$ but are different when $Re_{\delta_k}$ is changed. The blue symbols correspond to $Re_{\delta_k}$ values of 421 and 431 whereas the red symbols correspond to $Re_{\delta_k}$ values of 484, 491 and 520. At higher $Re_{\delta_k}$, the total disturbance energy decreases more rapidly in the near-wake region, reaches a smaller minimum value and then grows more rapidly than at lower $Re_{\delta_k}$.

Additional work conducted as part of AFOSR Project FA9550-05-1-0048 includes a study of receptivity and growth over distributed roughness and simultaneous measurements of $U'$ and $W'$ disturbances produced by a spanwise roughness array. Results for the distributed roughness experiment

are presented in the final report for Project FA9550-05-1-0048 and by Downs and White (2008). The $U'$, $W'$ data are used as part of the current-year effort to quantify transient growth receptivity.

### 1.3  Objective and Overview

The present work, AFOSR Project FA9550-07-1-0312, is a one-year conclusion of AFOSR Project FA9550-05-1-0048. The focus of both is the receptivity of stationary transient disturbances to surface roughness. The work reported here aims to provide a rigorous quantification of receptivity to a spanwise array of cylindrical roughness elements as pictured in Fig. 1. To achieve this, measurements of $U'$ and $W'$ obtained in the elements' wakes under project FA9550-05-1-0048 are analyzed using a biorthogonal decomposition procedure developed by Tumin (2003). There are a number of difficulties with applying Tumin's method directly to experimental data. Principally, the data is affected by measurement uncertainty and only some of the needed disturbance components are available in the experiment. Both of these issues are addressed. As additional tasks, the experimental data is further compared to the DNS results by Rizzetta and Visbal (2007) and the DNS data is subjected to the same biorthogonal decomposition as the experimental data. The comparisons reveal significant differences between the $W'$ and $V'$ obtained in the experiment and the DNS. These disturbance components represent the initial condition of transient growth and are thus critical inputs to a receptivity analysis.

## 2  Receptivity and Decomposition into Modes

### 2.1  Discrete and Continuous Modes

TS waves represent discrete eigenmodes of the OS system. At a specified frequency, spanwise wavenumber and $Re_\delta$, a discrete eigenmode exists with a certain complex-valued streamwise wavenumber $\alpha$ and complex-valued wall-normal mode shapes for the velocity and pressure perturbations. The complex $\alpha$ allows for both a streamwise wavelength and exponential growth or decay in the streamwise direction; the complex mode shapes allow for phase variations in the wall-normal direction.

Transient disturbances are fundamentally different that TS disturbances. In the transient growth scenario, one specifies a frequency (which may be $\omega = 0$ to represent stationary disturbances), a spanwise wavenumber $\beta$ and $Re_\delta$ and may find that no exponentially growing solutions exist; only decaying modes can be identified. Nevertheless, *algebraically* growing disturbances may still be observed. The reason is that the OS system admits a continuous spectrum of eigensolutions in addition to the discrete solutions that are manifested as TS waves. Transient disturbances are composed of all the modes of the continuous spectrum each of which has a particular complex amplitude. Because the OS system is not self-adjoint, the various continuous modes are not orthogonal. So, in spite of the fact that all the continuous modes decay, their non-orthogonality allows for some transient algebraic growth prior to eventual exponential decay (Schmid and Henningson 2001; Reshotko 2001).

The continuous spectrum of disturbances that produces transient growth arises from the correct treatment of the OS equations far from the wall at $y = 0$. The OS equations follow from the Navier–Stokes equations linearized about a parallel flow basic state:

$$\frac{\partial u'}{\partial x} + \frac{\partial v'}{\partial y} + \frac{\partial w'}{\partial z} = 0 \tag{1}$$

$$\frac{\partial u'}{\partial t} + U\frac{\partial u'}{\partial x} + v'\frac{\partial U}{\partial y} = -\frac{\partial p}{\partial x} + \frac{1}{Re_\delta}\nabla^2 u' \tag{2}$$

$$\frac{\partial v'}{\partial t} + U\frac{\partial v'}{\partial x} = -\frac{\partial p}{\partial y} + \frac{1}{Re_\delta}\nabla^2 v' \tag{3}$$

$$\frac{\partial w'}{\partial t} + U\frac{\partial w'}{\partial x} = -\frac{\partial p}{\partial z} + \frac{1}{Re_\delta}\nabla^2 w' \tag{4}$$

where $U = U(y)$ and $u'$, $v'$, $w'$ and $p'$ are linear perturbations. Applying Fourier transforms in $x$, $z$ and $t$ allows the vector of disturbance quantities to be written as

$$\phi = \hat{\phi}(y)\exp[i(\alpha x + \beta z - \omega t)] + \text{c.c.} \tag{5}$$

where $\phi = (u', \partial u'/\partial x, v', p', w', \partial w'/\partial x)^T$ and c.c. represents the complex conjugate of the preceding term. This allows Eqns. (1)–(4) to be represented as

$$\frac{d\hat{\phi}}{dy} = A\hat{\phi} \tag{6}$$

where the components of $A$ are functions of $\alpha$, $\beta$, $\omega$, $Re_\delta$, and $U(y)$. In the spatial problem, $\alpha$ is unknown so solving Eqn. (6) for $\hat{\phi}(y)$ and $\alpha$ is an eigenvalue problem.

In order to solve the eigenvalue problem to find discrete TS wave solutions, one iterates to find $\alpha$, $\hat{\phi}(y)$ pairs that satisfy Eqn. (6) subject to no-slip and no-penetration boundary conditions at the wall and a condition that $\hat{\phi}$ approaches zero as $y$ approaches infinity. The solutions are referred to as discrete because only certain isolated points in the complex $\alpha$ plane are solutions.

A more general solution to Eqn. (6) can be found if the boundary condition as $y$ goes to infinity is relaxed. The discrete mode solutions require $\hat{\phi}$ to approach zero as $y$ goes to infinity. However, the physical boundary condition that disturbances decay as $y$ increases can be satisfied through a superposition of many disturbances that do not decay. That is, instead of seeking a single solution to Eqn. (6) that satisfies the boundary condition $\hat{\phi} \to 0$, one can seek a set of solutions that collectively satisfy that boundary condition while each member of the set only satisfies $|\hat{\phi}| < \infty$.

The effect of the relaxed boundary condition on solutions to Eqn. (6) can be seen most clearly outside the boundary layer as $y$ goes to infinity. In this limit, $U(y)$ is constant so the equation has constant coefficients and its solutions $\hat{\phi}$ take the form

$$\hat{\phi}(y) = \tilde{\phi}\exp(\lambda y) \tag{7}$$

where the $\tilde{\phi}$'s are constants. The six $\lambda$'s that result from this approach are

$$\lambda_1 = -\sqrt{\alpha^2 + \beta^2} \tag{8}$$

$$\lambda_2 = +\sqrt{\alpha^2 + \beta^2} \tag{9}$$

$$\lambda_{3,5} = -\sqrt{i(\alpha - \omega)Re_\delta + \alpha^2 + \beta^2} \tag{10}$$

$$\lambda_{4,6} = +\sqrt{i(\alpha - \omega)Re_\delta + \alpha^2 + \beta^2} \tag{11}$$

where the branch cut of the square root function is selected such that the real part of the square root is positive. Discrete solutions only contain the odd-numbered $\lambda$'s because only these three go to zero as $y$ goes to infinity. However, for the relaxed boundary condition, the solutions need not decay
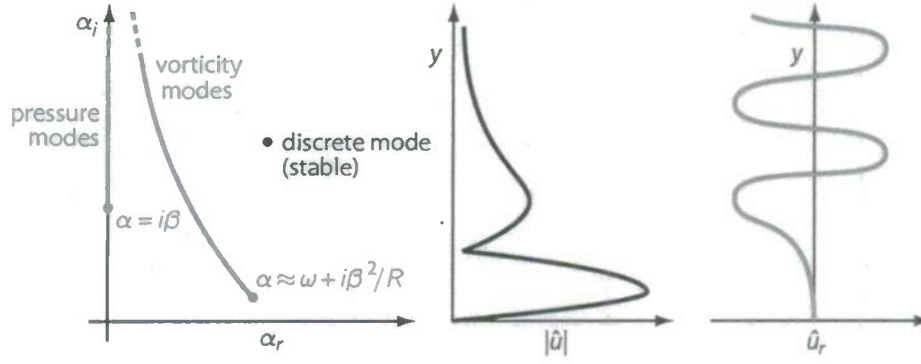
6

Figure 3: Schematic diagram of complex eigenvalues $\alpha$ (left); the discrete TS mode (middle) and the real part of a continuous-spectrum mode (right).

to zero but may remain at finite amplitude. Thus, the $\lambda$ values can be purely imaginary and, from Eqn. (7), this alternative produces solutions that undergo fixed-amplitude oscillations in $y$ outside the boundary layer.

To investigate the behavior of the oscillatory solutions, $\lambda$ values are parameterized as $\lambda = ik$ where $k$ is a real parameter that represents the wavenumber of the wall-normal oscillation. The first two solutions $\lambda_1$ and $\lambda_2$ are referred to as pressure modes because they are associated with non-zero pressure perturbations outside the boundary layer; the other modes are referred to as vorticity modes because they are associated with non-zero vorticity perturbations outside the boundary layer. Figure 3 is a schematic representation of the complex $\alpha$ values that result upstream of the TS waves' minimum critical Reynolds number. The red curves represent the pressure and vorticity modes; the black dot indicates the least-stable discrete TS wave. The pressure and vorticity solutions branches are referred to as branches of the continuous spectrum because each value of $k$ is associated with a particular disturbance amplitude. The dots at the ends of the red curves represents $\alpha$ when $k = 0$. The curves move toward larger $\alpha_i$ as $k$ increases. The imaginary part of $\alpha$ is the decay rate so higher-$k$ disturbances decay faster than lower-$k$ disturbances and pressure modes decay faster than vorticity modes because $Re_\delta$ is large. It is notable that when the disturbance of interest is stationary, $\omega = 0$, the vorticity branch collapses onto the pressure branch. Also notable is the very slow decay rate of the $k = 0$ vorticity mode.

Returning to the notion that a physical disturbance (which decays to zero as $y$ goes to infinity) can be represented by a superposition of discrete modes plus the continuous spectrum modes, the physical disturbance $\phi$ associated with a particular frequency and spanwise wavenumber can be represented by

$$\phi(x, y, z, t) =$$
$$\frac{1}{2\pi} \sum_{p,\omega} \int_k C(\alpha(k)) \, \hat{\phi}(y, \alpha(k)) \, \exp[i \, (\alpha(k)x + \beta z - \omega t)] \, dk$$
$$+ \frac{1}{2\pi} \sum_j C_j \, \hat{\phi}_j(y) \, \exp[i \, (\alpha_j x + \beta z - \omega t)] + \text{c.c.} \tag{12}$$

In this expression, the $C$ values are complex amplitudes of each of the modes and the indicies $p$, $\omega$ and $j$ represent the pressure branch, the vorticity branch and the index of the discrete modes, respectively. The solution of the eigenvalue problem gives $\hat{\phi}$ and $\alpha$ for each $k$ or $j$. Those calculations do not give the amplitude coefficients $C$; those values would be predicted by a receptivity theory (if one existed)

or should be measured in an experiment via a decomposition of $\phi$ data using an inverse transform of Eqn. (12). (This is the topic of Sec. 2.2.) Then, because the downstream disturbance evolution is controlled by the decay rates $\alpha$, the $C$ values representing the initial disturbance are sufficient to fully describe the downstream disturbance evolution.

As described earlier, *optimal* transient disturbances have been identified by Andersson et al. (1999), Luchini (2000) and Tumin and Reshotko (2001) to be stationary disturbances with $\beta = 0.45$. These disturbances are initially counter-rotating streamwise-oriented vortices that induce streamwise-oriented streaks of low-speed and high-speed fluid. The optimal disturbance represents one particular collection of complex amplitudes for the continuous spectrum modes. The experiments by White (2002) and White et al. (2005) establish that roughness-induced disturbances are not optimal; roughness-induced disturbances must be represented by a collection of continuous-mode amplitudes that differs from the optimal amplitudes. However, prior to this project this difference has never been quantified and no receptivity theory describes how particular roughness features might affect the continuous mode amplitudes. If such a theory existed, it might be possible to predict the nature of the transient growth resulting from a particular roughness configuration. The result would be a clearer link between stability theory and experimental measurements of transient growth. Thus, the over-arching objective of this project is to provide input data to the decomposition, the $\phi$ of the right-hand side of Eqn. (12), and to attempt a decomposition that gives $C(\alpha)$ for that configuration.

## 2.2   Receptivity Analysis and Biorthogonal Decomposition

The theoretical basis for decomposing disturbances into non-orthogonal sets of $\hat{\phi}(y)$ modes has been established by Zhigulev and Tumin (1987), Tumin et al. (1996) and Tumin (2003). This project follows Tumin's approach, particularly the 2003 paper. The challenging aspects of this arise from the facts that the modes are not orthogonal and that they are functions of a continuously varying parameter $k$. To begin, experimental data is collected in physical space $(x, y, z, t)$ and Fourier transforms in $z$ and $t$ are performed to give complex wall-normal mode shapes for particular $\beta$, $\omega$ pairs. These mode shapes are to be decomposed into the set of continuous modes $\hat{\phi}(y, \alpha)$. Because the modes are the non-orthogonal solutions to the OS equation, the *adjoint* OS equation must be developed and solved to give a continuous set of adjoint eigenmodes, $\hat{\psi}(y, \alpha)$. Then, the experimental data must be projected onto the $\hat{\phi}$'s by evaluating inner products of the data with these adjoint eigenmodes. The projection results in the $C$ values that are the amplitudes of each of the $\hat{\phi}$ modes in Eqn. (12).

To perform the biorthogonal decomposition, Tumin (2003) lays out a several-step procedure. To begin, it is necessary to calculate the adjoint eigenmodes. These modes are solutions of

$$\frac{d\hat{\psi}}{dy} = -\boldsymbol{A}^T \hat{\psi} \tag{13}$$

where $\boldsymbol{A}$ is the OS matrix operator that appears in Eqn. (6) and $T$ stands for transpose. The eigenvalues $\alpha$ resulting from adjoint problem, Eqn. (13), are the same as those of the direct problem, Eqn. (6).

Once the $\hat{\psi}$ functions are generated, the biorthogonality relationship between $\hat{\phi}$ and $\hat{\psi}$ must be developed. To do this, the six-component disturbance vector $\hat{\phi}$ is expanded to nine components, the original six plus $\partial\hat{u}'/\partial x$, $\partial\hat{v}'/\partial x$, and $\partial\hat{w}'/\partial x$ (the hats on the disturbance quantities indicate that these are Fourier transforms in $z$ and $t$) and $\boldsymbol{A}$ is split into two $9 \times 9$ matrices:

$$\boldsymbol{A} = \boldsymbol{A}_1 + i\alpha\boldsymbol{A}_2. \tag{14}$$

These steps avoid nonlinearities in $\alpha$ by eliminating explicit second derivatives with respect to $x$. To develop the orthogonality relationship, the expanded terms are combined in an inner product between $\hat{\phi}$ evaluated at wavenumber $\alpha$, $\hat{\phi}_\alpha$, and $\hat{\psi}$ evaluated at wavenumber $\alpha'$, $\hat{\psi}_{\alpha'}$. For later convenience, the inner product is weighted by $\exp(-\epsilon y^2)$, a function that goes to one as $\epsilon$ goes to zero. All this gives

$$\int_0^\infty \hat{\psi}_{\alpha'}^T \mathbf{A} \hat{\phi}_\alpha \; e^{-\epsilon y^2} dy. \tag{15}$$

Introducing the expanded form of $\mathbf{A}$, integrating by parts and applying Eqn. (13) yields

$$\frac{2i\epsilon}{\alpha' - \alpha} \int_0^\infty \hat{\psi}_{\alpha'}^T \hat{\phi}_\alpha \, y e^{-\epsilon y^2} dy = \int_0^\infty \hat{\psi}_{\alpha'}^T \mathbf{A}_2 \hat{\phi}_\alpha \, e^{-\epsilon y^2} dy. \tag{16}$$

This equation shows that as $\epsilon$ goes to zero, the left-hand side equals zero when $\alpha \neq \alpha'$. Thus, $\hat{\phi}$ and $\hat{\psi}$ are orthogonal and the orthogonality relationship only depends on $\mathbf{A}_2$. When $\alpha = \alpha'$, the left hand side must be evaluated in the limit of $\epsilon$ and $\alpha' - \alpha$ going to zero. The value of the left-hand side in that limit is $Q(\alpha)$, a function that also depends implicitly on $\beta$, $\omega$, $Re_\delta$, and $U(y)$. The function $Q(\alpha)$ represents the normalization constants of the biorthogonal decomposition.

With all this background established, the $C(\alpha)$ of an experimentally measured disturbance can be established by taking the inner product of the measured data obtained at some $x$ location, $\hat{\phi}|_x$, with $\hat{\psi}_\alpha$ at all values of $\alpha$ along the branches of the continuous spectrum:

$$C(\alpha) = \frac{1}{Q(\alpha)} \int_0^\infty \hat{\psi}_\alpha^T \mathbf{A}_2 \hat{\phi}|_x \, dy. \tag{17}$$

Because $Q(\alpha)$ has already been evaluated in the limit $\epsilon \to 0$ and because $\hat{\phi}|_x$ goes to zero as $y$ goes to infinity, there is no need for the $\exp(-\epsilon y^2)$ weighting function. It is possible to manipulate this expression and return to the six-component form of the disturbance vectors and adjoint. This form of the inner product is

$$C(\alpha) = \frac{-i}{Q(\alpha)} \int_0^\infty \hat{\psi}_\alpha^T \frac{\partial \mathbf{A}}{\partial \alpha} \hat{\phi}|_x \, dy. \tag{18}$$

Thus, the nine-component forms of the disturbances are only needed for intermediate steps in the theoretical development; they are not needed for the evaluation of experimental data.

Evaluating Eqn. (18) is the rigorously correct means of analyzing the receptivity of the boundary layer to input disturbances. The $C(\alpha)$ on the branches of the continuous spectrum give the amplitude of a disturbance at the streamwise position $x$ at which the disturbance is measured. Combined with the subsequent growth or decay of each of the modes, the $C$'s also predict the downstream disturbance evolution. To the extent that the linear-disturbance and parallel-flow assumptions are correct, the $x$ location at which Eqn. (18) is evaluated is not important; any location would produce equivalent results. However, because $Re_\delta$ is increasing with $x$, deviations from the predictions should be expected to increase with distance downstream from the evaluation location.

## 2.3   Receptivity Analysis with Partial Data

When experimental data is used as the input to Eqn. (18), two difficulties immediately arise. First, experimental data is uncertain and noisy so uncertainty propagates into the $C(\alpha)$. So, although the $C(\alpha)$ will perfectly reproduce a measured disturbance at the evaluation location, the downstream disturbance evolution may not be correctly predicted by the $C(\alpha)$. Therefore, it is necessary to assess

the impact of experimental uncertainty on Eqn. (18) and disturbance-growth predictions. This activity is beyond the scope of the present work but is being carried out as a follow-on activity.

A second, more immediate difficulty of using experimental data is that not all disturbance components can be measured. The streamwise disturbance $u'$ and its derivative $\partial u'/\partial y$ are straightforward to measure. The spanwise disturbance $w'$ and its wall-normal derivative have also been measured as part of the previous phase of this project (AFOSR Project FA9550-05-1-0048). However, $v'$ and $p'$ are essentially unmeasurable, especially for stationary disturbances. Luckily, in spite of having only partial data, it is still possible to evaluate Eqn. (18) using an approach suggested by Tumin et al. (1996). The basic idea is to replace unmeasured components of the $\hat{\phi}|_x$ input disturbance vector with appropriate scalar components of Eqn. (12). This approach also assumes that only the vorticity mode of the continuous spectrum contributes to the measured disturbance. For a case in which $u'$ and $w'$ are measured but $v'$ and $p'$ are not, the disturbance vector is given by

$$
\hat{\phi}|_x = \begin{pmatrix}
\hat{u}|_x \\
\partial\hat{u}/\partial y|_x \\
\int C(\alpha(k))\,\hat{\phi}_v(\alpha(k))\,dk/2\pi \\
\hat{w}|_x \\
\partial\hat{w}/\partial y|_x \\
\int C(\alpha(k))\,\hat{\phi}_p(\alpha(k))\,dk/2\pi
\end{pmatrix}.
\tag{19}
$$

where $\hat{\phi}_v(\alpha(k))$ and $\hat{\phi}_p(\alpha(k))$ represent the $v'$ and $p'$ components of the $\hat{\phi}(\alpha(k))$ mode, respectively.

When Eqn. (19) is substituted into Eqn. (18), the unknown $C(\alpha)$'s appear on both sides of the equation. To account for this, individual terms on the right-hand side of Eqn. (18) that contain $C(\alpha)$ must be extracted and moved to the left-hand side. For unknown $v'$ and $p'$, the result is

$$
C(\alpha) - \frac{1}{2\pi Q(\alpha)} \iint C(\alpha(k)) \left[ Re_\delta\,\hat{\psi}_2(y,\alpha(k))\hat{\phi}_p(y,\alpha(k)) \right.
$$
$$
\left. + \left(\frac{2i\alpha}{Re_\delta} - iU(y)\right) \hat{\psi}_4(y,\alpha(k))\hat{\phi}_v(y,\alpha(k)) \right] dk\,dy
$$
$$
= \frac{1}{Q(\alpha)} \int \left\{ \left[ (Re_\delta\,U(y) - 2i\alpha)\,\hat{\psi}_2(y,\alpha) - \hat{\psi}_3(y,\alpha) \right] \hat{u}(y) \right.
$$
$$
\left. - \frac{1}{Re_\delta}\hat{\psi}_4(y,\alpha)\frac{\partial\hat{u}}{\partial y} + (Re_\delta U(y) - 2i\alpha)\,\hat{\psi}_6(y,\alpha)\hat{w}(y) \right\} dy.
\tag{20}
$$

This expression is evaluated at a particular $\alpha$ to give $C$ at that $\alpha$. However, the left-hand side includes integrals over $C(\alpha(k))$ so a straightforward solution is not possible. Instead, the integrals are replaced with sums over $N$ discrete values of $k$ that approximate the continuous spectrum. Defining $C_n = C(\alpha(k_n))$, Eqn. (20) becomes

$$
(I - L)\,C = R
\tag{21}
$$

where the $N \times N$ matrix $L$ represents terms that include $C(\alpha(k))$ to account for unmeasured disturbance components, $I$ is the identity matrix, $C$ is the length-$N$ vector of unknown $C(\alpha(k_n))$'s and $R$ is a length-$N$ vector of the right-hand side terms. Solving Eqn. (21) requires inverting $(I - L)$. The less is known about the input disturbance, the closer this matrix will be to singular. Thus, the less is known about the input disturbance, the more prone this process is to amplifying experimental errors.

# 3   Measurement and Analysis of $W'$ and $V'$

The previous sections make clear that to perform a rigorous receptivity analysis using experimental data, it is necessary to measure as many of the disturbance components as possible with as much accuracy as possible at some $x$ location downstream of the disturbance source. To this end, measurements of disturbances generated by a spanwise array of cylindrical roughness elements were completed previously during AFOSR Project FA9550-05-1-0048. Streamwise and spanwise components of the roughness-induced stationary disturbances were measured in multiple spanwise/wall-normal planes and this data was used to estimate the wall-normal disturbance velocity using the continuity equation. In this section, the approach to these measurements and estimates of experimental uncertainty are given. The following section gives results for the biorthogonal decomposition of this data.

## 3.1   Wind tunnel, instrumentation, flat plate and roughness

The wind tunnel facility used for the experiments was the Case Western Reserve University (Case) wind tunnel, an open-return facility with a 710 mm × 710 mm × 2.7 m test section and a maximum operating speed of 25 m/s. The tunnel's design follows the recommendations of Reshotko et al. (1997) for flow quality. Operating at 12 m/s, the total (not high-pass-filtered) $u'_{rms}$ level in the test section is approximately $0.35\% \, U_\infty$. Although this level may seem high relative to other tunnels, fluctuation spectra indicate that approximately 93% of the fluctuation power is contained below 1 Hz, a conservative cutoff frequency for AC-coupling filters. To compare the fluctuation measurements of the Case tunnel to facilities whose quoted turbulence levels are measured using traditional AC-coupled fluctuation-intensity measurements, only the $u'$ intensity above 1 Hz should be considered. Restricted to these frequencies, the Case tunnel's $u'_{rms}$ level is $0.09\% \, U_\infty$. Alternatively, separating the contributions of acoustic and turbulent velocity fluctuations in the manner suggested by Reshotko et al. (1997) shows that the turbulent $u'_{rms}$ amounts to $0.05\% \, U_\infty$.

Velocity measurements are made using 2.5-$\mu$m-diameter hotwire probes. Streamwise velocity measurements are made concurrently in the boundary layer and the freestream. The velocity measured by the boundary layer probe is normalized on a point-by-point basis by the freestream velocity $U_\infty$ to give a nondimensional boundary layer velocity. Measurement of the flow field is accomplished by collecting data in dense 2D grids at varying streamwise locations. The motion of hotwire probes is controlled by an externally mounted traverse that provides approximately 1200 mm of travel in the streamwise direction $(x)$, 190 mm of travel in the spanwise direction $(z)$ and 70 mm of travel in the wall-normal direction $(y)$. The stepper motors that drive the traverse provide this motion in steps of 3.2 $\mu$m, 1.6 $\mu$m and 1.6 $\mu$m, respectively.

The flat plate model was originally constructed by Reshotko and Leventhal (1981). The model is mounted vertically in the tunnel 0.5 m downstream of the test section inlet, with the test side located approximately 250 mm from test section's side wall. The plate is constructed of aluminum and is 9.5 mm thick, 635 mm in span, and 1100 mm in length. The plate's leading edge is elliptical with the flat portion of the plate beginning 25 mm from the leading edge. A hinged trailing-edge flap is used to ensure that the incoming flow stagnates on the test side of the plate. The test side of the plate is polished to a near-mirror finish.

The roughness array that generates the stationary disturbances is described by Ergin and White (2005). Briefly, the setup is the same as is pictured in Fig. 1 with $x_k = 300$ mm ($x_{v.l.e.} = -7$ mm), a spanwise spacing of $\lambda_k = 19$ mm, a diameter $d = \lambda_k/3$ and an amplitude of $Re_k = 202$. For these measurements the unit Reynolds number is $Re' = 764 \times 10^3$ m$^{-1}$.

## 3.2 Hotwire measurement techniques and results

Measurements are performed by hotwire anemometers that are moved through spanwise–wall-normal planes oriented as shown in Fig. 1 at various $x$ locations. The hotwires are moved through 38 0.5-mm spanwise steps per 19-mm roughness wavelength, $\lambda_k$. This permits spatial phase-lock averaging to be performed on the data in order to minimize random variations in the steady velocity field.

Streamwise velocity measurements are obtained using straight-wire probes and are decomposed into a spanwise-invariant basic state, a stationary disturbance and an unsteady disturbance as

$$u(x, y, z, t) = \overline{U}(x, y) + U'(x, y, z) + u'(x, y, z, t). \tag{22}$$

The basic state profile $\overline{U}$ is computed by spanwise phase-locked averaging the steady velocity profiles measured at $z$ locations that are judged to be outside the influence of upstream roughness. This averaged profile is expected to be least affected by the roughness and most representative of Blasius flow.

Boundary-layer integral quantities, $\delta^*$ and $\theta$ are computed from basic-state profiles at each $x$ and these measurements are used to verify the plate's alignment for zero pressure gradient and to nondimensionalize the wall-normal coordinate as $\eta = y/\delta$. First, a zero-pressure-gradient condition is verified by the shape factor $H = \delta^*/\theta$ falling in the range $2.59 \pm 0.05$ (Saric 2007). If this is verified, the boundary-layer thickness scale $\delta$ is given by $\delta = \delta^*/1.7208$ and $\delta = \theta/0.664$. For each experimental configuration, a nonlinear least squares fit is performed to the $\delta(x)$ data resulting from both $\delta^*$ and $\theta$ as

$$\delta(x) = \left( \frac{x - x_{\text{v.l.e.}}}{Re'} \right)^{1/2} \tag{23}$$

where the fit parameters are $x_{\text{v.l.e.}}$, the virtual leading edge location, and $Re'$, the unit Reynolds number, $U_\infty/\nu$. Uncertainties are known for the experimental $\delta$ values so uncertainties are computed for the fit parameters. Applying these values allows calculation of boundary-layer and roughness parameters and those parameters' uncertainties at any $x$ location.

Because spanwise-periodic roughness is used, velocity profiles measured aft of the roughness can be phase-locked averaged using the periodicity $\lambda_k$. This process results in a representative flow field for one roughness array length. The steady boundary layer disturbance is defined as the deviation from the basic state. Thus, the steady disturbances $U'(\eta, z)$ are computed by subtracting the basic state profile from each of the other averaged profiles obtained behind the roughness. To collapse this steady disturbance field to a single profile that is representative of the overall flow disturbance the roughness creates, the root-mean-square of the steady disturbance profiles is taken in the spanwise direction. The result is a single disturbance profile, $U'_{\text{rms}}(\eta)$. The total disturbance energy associated with the streamwise disturbance component is quantified as the wall-normal integral of this profile squared:

$$E_{\text{rms}}^{(U)} = \int_0^\infty \left[ U'_{\text{rms}}(\eta) \right]^2 d\eta. \tag{24}$$

Equivalent measures of the total disturbance energy associated with the $V'$ and $W'$ components would be $E_{\text{rms}}^{(V)}$ and $E_{\text{rms}}^{(W)}$, respectively. In practice, this integration is carried out using a simple trapezoidal integration scheme. The upper limit of integration is in the freestream where the disturbance profile is close to zero. Typically, $\eta$ values of 10 to 12 are used for this purpose. The overall total disturbance energy is the sum of the three components.

Although the total streamwise disturbance energy is a useful means of quantifying the streamwise

disturbance evolution, it gives no information as to the behavior of individual spanwise wavelengths in the velocity disturbance field and how these wavelengths might be connected to the roughness. To examine these details, the $U'(\eta, z)$ disturbances are transformed using a spatial Fourier transform in the spanwise direction to give $\hat{U}(\eta, \beta)$. This operation is completed using two roughness patches as a spanwise sampling length. Overlapping four such transforms by 50% and complex-averaging the results achieves the optimal reduction in the variance (Press et al. 2001).

After performing the Fourier transforms, the power spectral density (PSD) of the signal is computed. The PSD is essentially $|\hat{U}|^2$ normalized such that:

$$[U'_{rms}(\eta)]^2 = \sum_{m=0}^{\infty} PSD(\eta, \beta_m). \tag{25}$$

The disturbance energy contained in any particular mode can be found in a manner similar to the total disturbance energy. The PSD component of interest is integrated in the wall-normal direction using a simple trapezoidal scheme:

$$E_{\lambda_k/m}^{(U)} = \int_0^{\infty} PSD(\eta, \beta_m) d\eta. \tag{26}$$

As a consequence of the PSD normalization, the total disturbance energy is equal to the sum of the disturbance energies in each of the integer modes:

$$E_{rms}^{(U)} = \sum_{m=0}^{\infty} E_{\lambda_k/m}^{(U)}. \tag{27}$$

Spanwise velocity measurements are obtained using a pair of slant-wire probes with different angular orientations at the same location. For this purpose, a hotwire sting is used that carries a combination of slanted and straight hotwire sensors (Fig. 4). This sting assembly includes a shaft that rotates in a streamlined casing and allows angular calibration of slanted hotwires. Outside the test section, the shaft is connected to an angle indicator and the sting assembly is rigidly attached to the traverse. Inside the test section, the hotwire sensors are placed perpendicular to the shaft's axis through a multiple-hotwire holder. The angular position of the sensors can be adjusted by rotating the spindle of the angle controller with a precision of $0.2°$. The multiple-hotwire holder is designed to carry four hotwires. One hotwire is a straight sensor in the freestream; the remaining three sensors are in the boundary layer. The boundary-layer sensors are positioned in a trident design with one straight sensor in the middle and two slanted hotwire sensors mounted 9.5 mm one either side of the the center probe. Using a separation that is an integer multiple of the spanwise step permits all three boundary layer sensors to be placed at the same measurement location at three different spanwise traverse steps. Naturally, this requires excellent alignment of the flat surface with the traverse plane and the sensors with respect to each other and great care is exercised to achieve this alignment.

Slanted hotwire angle calibration is performed following the recommendations of Bruun (1995). First, the yaw angle of each wire is determined by gradually rotating the sensor in the freestream and monitoring the bridge voltage. When the bridge voltage is a maximum, the maximum cooling rate is achieved because the impinging velocity is perpendicular to the wire axis. The calibration of all four sensors is performed simultaneously. First, the sting is positioned so that all hotwires are located in the freestream. Second, it is rotated 5° clockwise from its position during an experiment and a velocity calibration is performed. Third, the sting is rotated 10° counterclockwise and another velocity calibration is performed for the same tunnel speed range. Finally, data from both velocity calibrations at two different angles are combined and the calibration constants are computed by using the King's
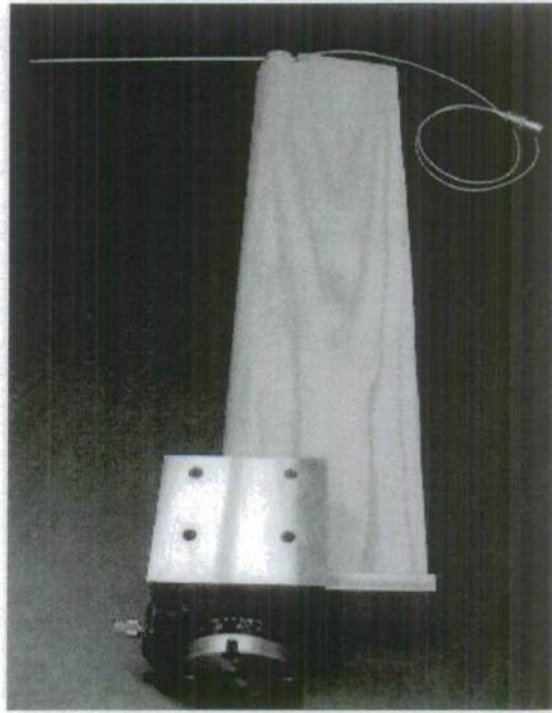
Figure 4: Multiple-probe hotwire sting with angular adjustment capability.

Law and Hinze's formula (Hinze 1959):

$$V_e = \left(A + B E^2\right)^n = \tilde{V} \left(\cos^2 \alpha + k^2 \sin^2 \alpha\right)^{1/2}. \tag{28}$$

In these equations $A$, $B$ and $n$ are calibration constants, $\tilde{V}$ is the freestream speed (during the calibration procedure only), $V_e$ is the effective cooling velocity, $E$ is the hotwire voltage, $\alpha$ is the sensor's yaw angle and $k$ is the sensor's yaw coefficient. A nonlinear least-square fit is performed to find $A$, $B$, $n$ and $k$ values for each sensor. The yaw coefficient is assumed to be constant following Jørgensen (1971). According to Bruun, this method predicts the effective cooling velocity to within 1% for yaw angles between 0° and 70° and the error reaches only 15% for a yaw angle of 90°.

In the present work, alignment tests showed the slant-wire $\alpha$ values to be $40.0° \pm 0.5°$. Typical values for the Hinze-formula constants are give in Table 1. Precise determination of the yaw coefficient, $k$ requires a very accurate knowledge of the wire angle, $\alpha$. Typical $k$ values for single yawed sensors reported in the literature are around 0.1. According to a study cited by Bruun (1995), the value of the calculated yaw coefficient $k^2$ is very sensitive to an assumed yaw angle error, $\sigma_\alpha$; a yaw-angle uncertainty as low as 1° can produce negative values for $k^2$, which is not physically possible. As noted above, the present yaw-angle uncertainty is 0.5°. There could, therefore, be considerable errors in $k$. Fortunately, the individual uncertainties from $\alpha$ and $k$ cancel in Hinzes formula, reducing the combined uncertainty on the right-hand-side to less than 1%.

Separating the effective cooling velocity, $V_e$, measured by the slanted sensors into $U$ and $W$ requires a careful treatment of the experimental data. First and foremost, since the two slanted sensors sweep different $(y, z)$ planes, the data from slanted sensors are shifted such that the slanted sensors spanwise locations match with those of the the middle sensor. Despite the effort to align the boundary layer

14

| Sensor | $A$ | $B$ | $n$ | $k$ |
|---|---|---|---|---|
| Freestream | −1.591 | 0.582 | 2.258 | − |
| Boundary Layer | −1.419 | 0.538 | 2.377 | − |
| Top Slanted | −1.546 | 0.551 | 2.328 | 0.160 |
| Bottom Slanted | −1.879 | 0.665 | 2.209 | 0.180 |

Table 1: Typical calibration constant values obtained during multicomponent experiments.

sensors with respect to the flat surface, the misalignment between the sensors cannot be avoided completely. This implies that each sensor is sweeping the boundary layer at a different height from the flat surface. However, the position of each sensor with respect to the flat surface is extremely important for multicomponent data analysis. To account for any misalignment of sensors in the wall-normal direction, the wall location is estimated for each sensor at between-roughness $z$ stations. This means that the effective cooling velocity data recorded by each sensor has a different $y$ array, and the $V_e$ data obtained from all three sensors must be interpolated onto a single array of heights. Once this is completed, the spanwise and streamwise velocities are resolved from the effective cooling velocity data obtained from the slanted sensors.

With the available streamwise and spanwise velocity components, the wall-normal velocity component, $V$ and the wall-normal velocity perturbation, $V'$, can be obtained by using the appropriate form of the continuity equation. The first order derivatives $\partial U/\partial x$ and $\partial W/\partial z$ in this equation are approximated by central differences and $V$ is estimated by numerically integrating $\partial V/\partial y$ using the no-penetration boundary condition at the wall: $V = 0$ at $y = 0$. Generating derivatives from experimental data is generally to be avoided as small differences between measurements points can easily be overwhelmed by measurement uncertainties at each of the points. Nevertheless, the approach taken here is seen as the most effective means of estimating $V'$ across the boundary layer. But, doing so requires that measurements in closely spaced $x$ planes be obtained.

The results of the multicomponent experiments include $U$, $V$, $W$, and $\Omega_x$, the steady streamwise vorticity, in the domain 310 mm $< x <$ 550 mm, 0 mm $< y <$ 4.7 mm and −9.5 mm $< z <$ 9.5 mm. The grid has variable spacing in the streamwise direction with $\Delta x$ as low as 2.5 mm in the near wake of the roughness array and gradually increasing to as high as $\Delta x = 50$ mm in the far wake. A typical phase-lock averaged steady flow can be seen in Fig. 5. In this figure, the streamwise flow is into the page, the abscissa is the spanwise direction and the ordinate is the wall-normal direction, both displayed in units of millimeters. The roughness element that generates the disturbance extends between −3.17 mm$< z <$3.17 mm and is 724 $\mu$m tall. The green contour lines indicate 10% increments of dimensionless streamwise velocity $U$, the vector field represent the dimensionless $V$ and $W$, and the colored contours represent the magnitude of the streamwise vorticity. The heavy horizontal line segment at the top right corner is equivalent to a velocity magnitude of 10% $U_\infty$. The colored contour levels that represent $\Omega_x$ are shown on the right-hand side of each figure and have the units of inverse millimeters. Warmer colors (yellow, orange, red, etc.) represent a positive streamwise vorticity (into the page), indicating a clockwise fluid rotation in these figures. Conversely, the colder colors (blue, turquoise etc.) represent negative streamwise vorticity (out from the page), indicating a counter-clockwise fluid rotation in the figures. White indicates zero streamwise vorticity.

Figure 5 and results at the other streamwise locations appear exactly as one would expect. In the near wake, the flow is decelerated behind the roughness element. Moving downstream, a pair of counter-rotating streamwise vortices strengthen and then decay. Meanwhile, the decelerated flow along the roughness-element centerline, $z = 0$, gradually becomes accelerated due to the action of

the streamwise vortices. This scenario is consistent with flow-visualization images by Gregory and Walker (1956) and the general transient-growth scenario. Integrating the $U'_{rms}$ and $W'_{rms}$ disturbances at each $x$ location gives the energy evolution curves shown in Fig. 6. These curves suggest that in the near wake of the roughness element, the $U'$ component has large energy while the $W'$ component starts with little energy and grows. Then, once the spanwise component energy has increased to an appreciable level, transient growth begins with decaying the streamwise vorticity associated with $W'$ component energy leading to algebraic growth of the $U'$ disturbance energy.

This description of the transient growth process was reported in the Final Report for AFOSR Project FA9550-05-1-0048. However, when efforts were made to compare the results in Fig. 5 to the DNS results by Rizzetta and Visbal (2007), it became apparent that the $W'$ component energy measured in the experiment greatly exceeded that calculated by the DNS. Given that the DNS results are thought to be valid (Denissen and White 2008), the most likely explanation for the discrepancy is a systematic measurement error that affects $W'$ but not $U'$. The $W'$ component is given by the difference (essentially) of the output of the two slant wires and, because the $W'$ component is very small, the difference is subject to large uncertainties. To better understand how measurement uncertainty may lead to systematically too-large $W'$ components, an extensive Monte Carlo simulation of the data analysis approach and measurement uncertainty was performed. This analysis is described below. The importance of properly resolving this point is driven by the biorthogonal decomposition with partial data. The more information is available about a disturbance (i.e., which components) and the more certain that information is, the better the resulting $C(\alpha)$ distribution will be as a predictor of disturbance evolution. The $W'$ data in question is especially important in this regard because it is the measurable component of $\Omega_x$, the initial streamwise vortex that gives rise to transient growth.

## 3.3 Monte Carlo analysis of measurement uncertainty

The hotwire measurement uncertainty is driven by two main factors: the uncertainty of the hotwires' calibration constants and the uncertainty of the wall location that is estimated as part of the data analysis. The hotwire voltages at each measurement point are not considered as sources of uncertainty because the mean voltage at each point is well resolved by long-duration samples. Nevertheless, the calibration uncertainty leads to velocity uncertainty at each point.

The initial approach to understanding the uncertainties of the $W'$ and other velocity components used a straightforward technique described by Bevington (1969). That is, uncertainties in calculated quantities are estimated by taking the partial derivatives of the calculated quantities with respect to each of the uncertain input quantities and summing derivatives squared multiplied by input disturbance variances. Including proper treatment of input quantity covariances, a calculated quantity $u$ that is a function of $x$ and $y$ has a variance (uncertainty squared) of

$$\sigma_u^2 = \left(\frac{\partial u}{\partial x}\right)^2 \sigma_x^2 + 2\left(\frac{\partial u}{\partial x}\frac{\partial u}{\partial y}\right)\sigma_{xy}^2 + \left(\frac{\partial u}{\partial y}\right)^2 \sigma_y^2 \tag{29}$$

where $\sigma^2$ terms are variances and $\sigma_{xy}^2$ is the covariance of $x$ and $y$. If $u$ was also a function of $z$, Eqn. (29) would include six terms, the three terms listed plus terms to account for $\sigma_z^2$, $\sigma_{xz}^2$ and $\sigma_{yz}^2$. The covariance terms are important because the hotwire calibration produces four constants per wire, $A$, $B$, $n$ and $k$, as well as four variance terms and six covariance terms.

The straightforward approach successfully estimated the uncertainty on the effective cooling velocity $V_e$ at each point but quickly bogged down with the more complex tasks of propagating uncertainties into the disturbance components and wall-normal integrals of these components. The fact that the un-
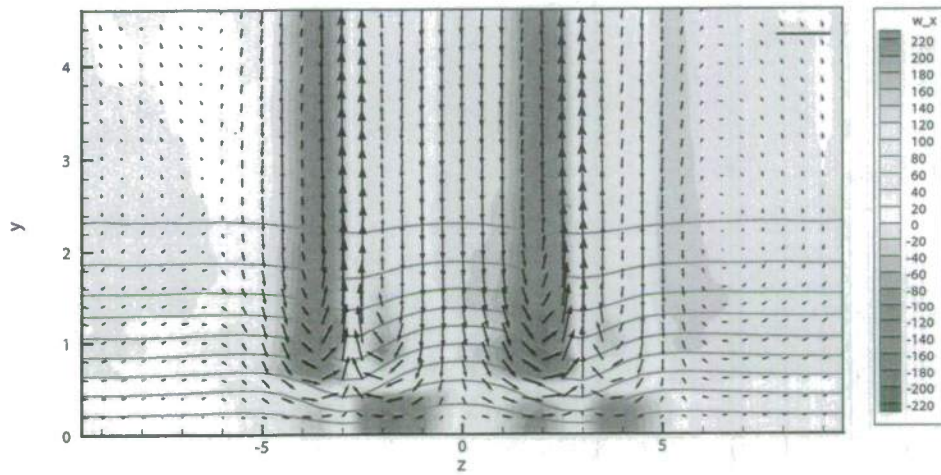
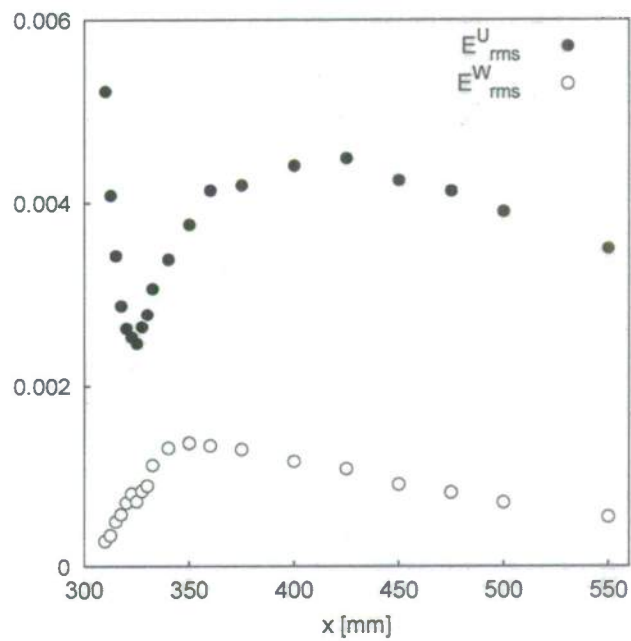Figure 5: Steady flow properties at $x = 350$ mm.



Figure 6: Total disturbance energies of the streamwise and spanwise velocity disturbance components.

certainty arises from the initial calibration makes the uncertainties of all the velocities highly correlated and this leads to massive and unworkable covariance expressions.

As an alternative approach, we have conducted a Monte Carlo simulation of the experiment to provide uncertainty estimates. The basis for this technique is to repeatedly analyze the raw experimental data with randomly selected parameter values drawn from probability distributions with the same characteristics as the uncertain parameters. That is, each day's calibration produced four calibration constants for each of the four hotwires and uncertainty estimates for each of those constants. Our approach is to repeatedly analyze the experiment not with the 16 calibration constants as measured but with 16 parameters drawn from Gaussian probability distributions with means equal to the 16 parameters and standard deviations equal to the parameters' uncertainties. Furthermore, we are careful to account for covariances so coupled uncertain quantities are treated correctly. By performing the data analysis hundreds or thousands of times for different hypothetical calibration sets, we are able to generate converged statistical outcomes of the experiment and use those to understand experimental uncertainty in the face of highly covariant data and nonlinear processes (e.g., the slantwire response and slantwire response differences to give $W'$).

Figure 7 shows a result of the Monte Carlo analysis process. In these plots, the original hotwire data was analyzed 500 times, each time using a different set of randomly selected hotwire calibration constants. The solid line profiles represent the $\lambda_k$ and $\lambda_{k/3}$ disturbance profiles of the $U'$ and $W'$ disturbances as calculated using the nominal set of hotwire calibration constants. The solid symbols represent the mean value of the 500 analyses and the error bars represent the standard deviation of the analyses about the mean. The mean of the $\hat{U}$ simulations are in good agreement with the results obtained using the nominal calibration constants. So, for the $\hat{U}$ data, the repeated analyses only serve to establish uncertainty information. Hypothetically, the actual set of hotwire calibration constants is one of the set represented by the 500 repeated analyses so the standard deviation bars indicate the probable range of the actual data. For the $\widehat{W}$ profiles, the mean of the analyses is slightly larger than the result obtained using the nominal value. This is likely a result of the strongly nonlinear equations for $W'$. Thus, for the $\widehat{W}$, the Monte Carlo approach results in a revised value for the best-estimate spanwise disturbance relative to the value generated from a straightforward calculation.

Combining all the spanwise disturbance modes (i.e., integrals of the profiles shown in Fig. 7) for repeated analyses gives histograms or probability distributions for the total disturbance energies. Such a plot is shown in Fig. 8 for $x = 400$ mm, the same location shown in Fig. 7. This shows a relatively wide range of possible energy outcomes corresponding to the range of possible hotwire calibration coefficients. This plot *does not* indicate that the $W'$ energy might exceed the $U'$ disturbance energy at $x = 400$ mm; the outputs are correlated and larger $U'$ disturbances tend to occur with larger $W'$ disturbances. What the plot *does* establish is that the range of probable total disturbance energy values are quite large relative to the energies' most-likely values. The positive skewness of the $W'$ disturbance energy distribution also reinforces the strongly nonlinear nature of the spanwise disturbance calculation.

Repeating the Monte Carlo analysis at all streamwise locations yields the streamwise and spanwise disturbance energy evolution with rigorous uncertainty estimates. Figure 9 shows the energy evolution resulting from a straightforward calculation plus the mean of 355 Monte Carlo analyses at each $x$ and 95% confidence intervals for the disturbance energy. (95% confidence intervals represent $\pm 1.96$ standard deviations.) First, it is obvious that the energies plotted in Fig. 9 exceed the energies resulting from the earlier straightforward analysis presented in Fig. 6. This is a result of a revised normalization standard that is more consistent with how DNS results are analyzed. The more significant point is that the Monte Carlo analysis *does not* appreciably change the spanwise component disturbance
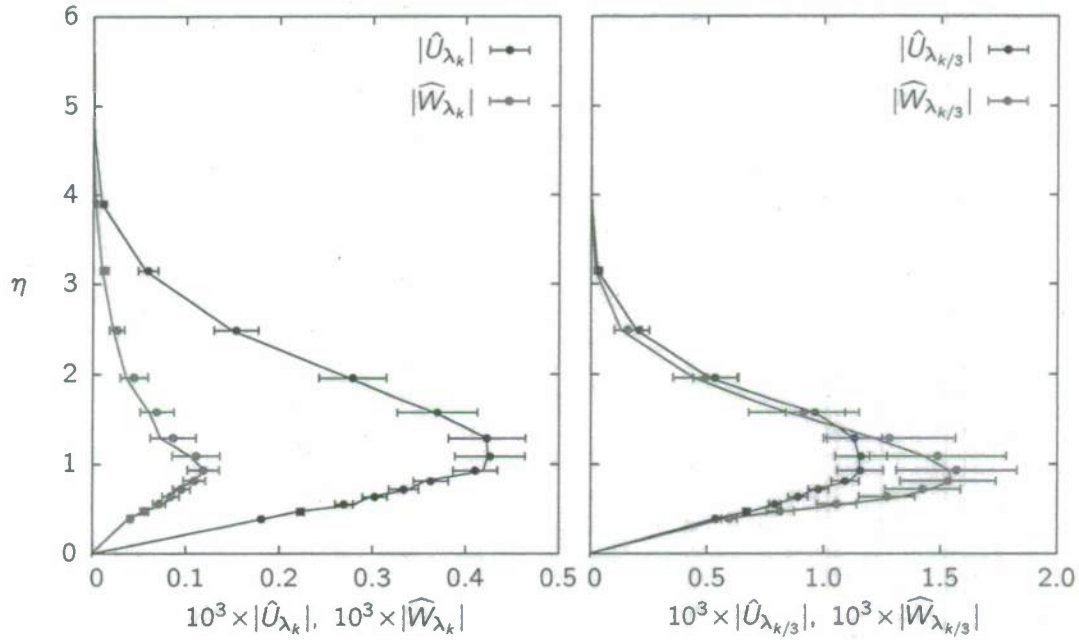
18

Figure 7: $\hat{U}$ and $\widehat{W}$ profiles at $x = 400$ mm for the $\lambda_k$ (left) and $\lambda_{k/3}$ spanwise disturbance modes. Solid lines are disturbance profiles generated using nominal hotwire calibration constants; symbols are the mean values of $N = 500$ analyses with randomly selected hotwire data; error bars are the standard deviations of the $N = 500$ analyses.
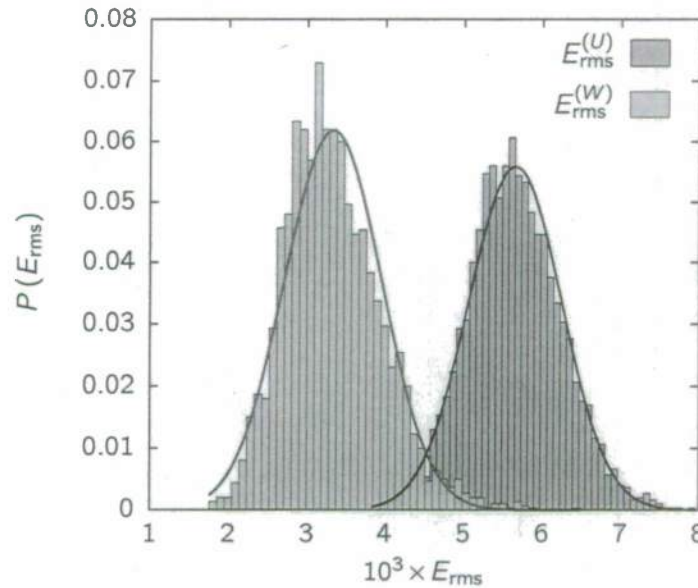


Figure 8: Total disturbance energies of the streamwise and spanwise disturbance components at $x = 400$ mm. Curves are normal distributions with means and standard deviations to match the histograms of $N = 3000$ analyses.
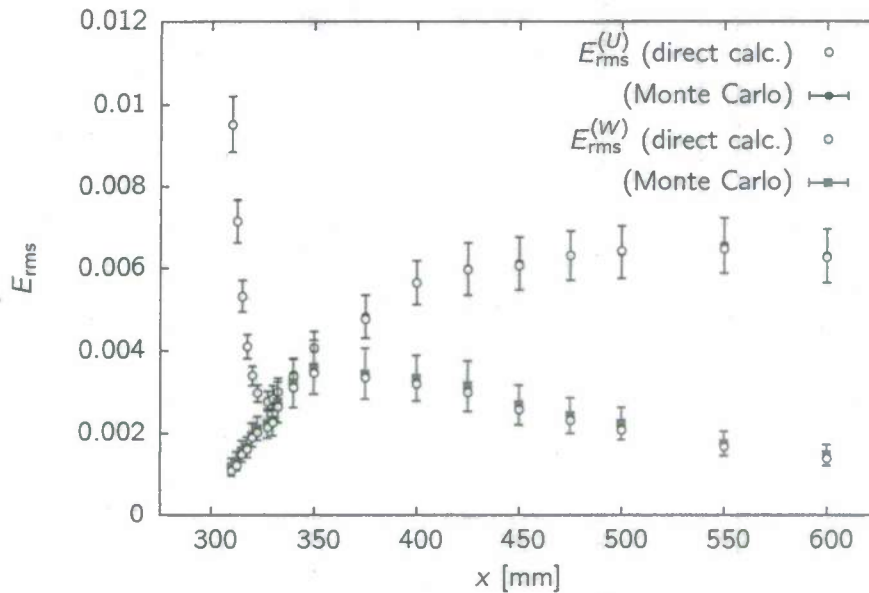
Figure 9: Streamwise evolution of the total disturbance energy of the streamwise and spanwise disturbance components. Monte Carlo results are the mean and 95% confidence intervals for 355 analyses.

energy. The experimentally measured values remain much higher than the equivalent DNS results by Rizzetta and Visbal (2007). Moreover, the uncertainty bounds on the spanwise disturbance energy do not include the energy calculated by the DNS. Thus, it is a strong possibility that a procedural error in the hotwire calibration or some other experimental protocol produces these erroneously large $W'$ disturbances. We are working to resolve this problem prior to publication of the results.

## 4 Biorthogonal Decomposition

In spite of the suspected error in the $W'$ data, it is possible to proceed with biorthogonal decomposition. For this, three approaches were implemented: decomposition of the DNS data by Rizzetta and Visbal (2007), partial-data decomposition of the experimental $U'$ data, and partial-data decomposition of the experimental $U'$ and $W'$ data.

DNS data lends itself particularly well to biorthogonal decomposition because full, accurate disturbance data is available on a fine grid. For this project, DNS data corresponding to $Re_k = 202$ and 339 roughness arrays was provided by Dr. Donald Rizzetta of AFRL. The simulation is described by Rizzetta and Visbal (2007); it is designed to simulate the experiments by Ergin and White (2006). The $Re_k = 202$ configuration has a relatively low level of unsteady disturbances and steady disturbances undergo transient growth. In the $Re_k = 339$ configuration, there are large unsteady fluctuations and the flow breaks down to turbulence about 100 mm downstream of the roughness array. Thus, the $Re_k = 202$ configuration is used here for decomposition.

To begin, data from $x = 325$ mm is selected. This position is sufficiently close to the roughness array at $x = 300$ mm to be in the near-wake receptivity region but not so close that strong disturbances that cannot be captured by the OS Equation corrupt the analysis. The time-averaged quantities making up the $\phi$ vector, $\phi = (u', \partial u'/\partial x, v', p', w', \partial w'/\partial x)^T$, are extracted from the data and spanwise Fourier transforms are performed to yield $\hat{\phi}(y)$ for each spanwise wavenumber $\beta$. The first four
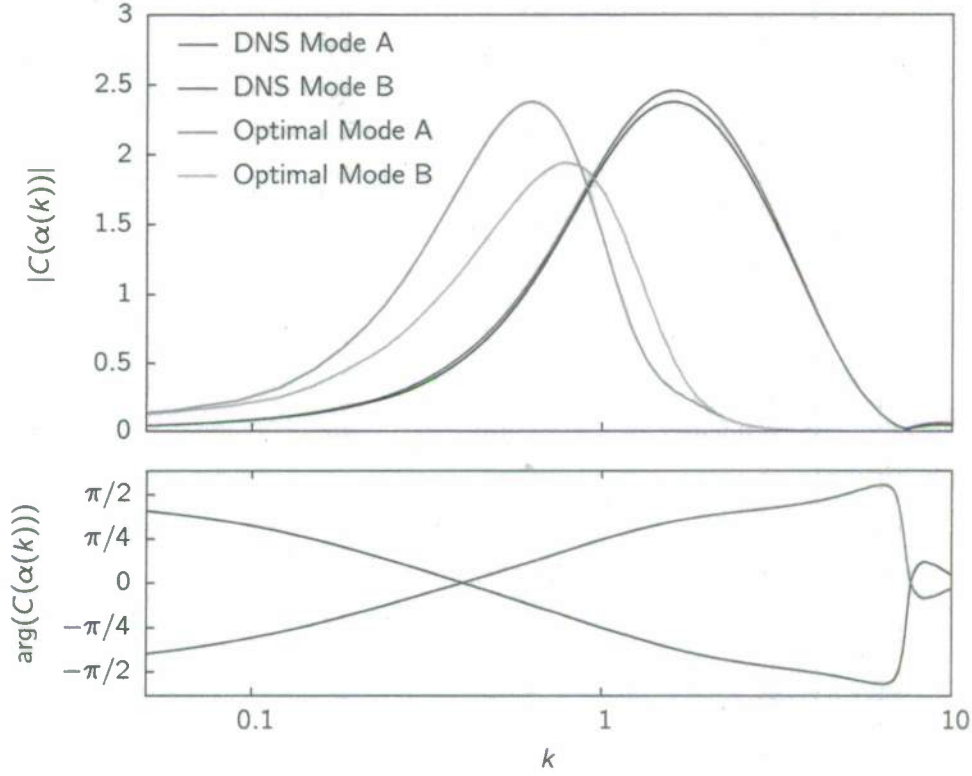
Figure 10: Amplitude (top) and phase (bottom) of the complex amplitudes of the A- and B-mode continuous spectra $C(\alpha(k))$ for the $\lambda_{k/3}$ mode obtained from the Rizzetta and Visbal (2007) DNS at $x = 350$ mm. The optimal disturbance modes for the same $\beta$ and $Re_\delta$ is shown for comparison.

spanwise modes, $\lambda_k$, $\lambda_{k/2}$, $\lambda_{k/3}$ (the roughness diameter) and $\lambda_{k/4}$, are used as the $\hat{\phi}|_x$ inputs to Eqn. (18). Each spanwise mode has a different $\beta$ and, therefore, a different $\alpha(k)$ distributions and $\hat{\psi}(y, \alpha(k))$ adjoint modes.

Equation (18) is solved numerically using a spectral technique using $2 \times 487$ vorticity modes as a discretized approximation of the continuous spectrum. There are two linearly independent vorticity branches called the A and B modes; each has 487 discrete solutions that are logarithmically distributed from $k = 0.01$ to 12.5. Results for the $\lambda_{k/3}$ mode's $C$ distribution are given in Fig. 10. This plot shows that the A and B mode amplitudes are nearly identical and their phases are nearly opposite. (A and B are linearly independent so no cancellation should be expected.) Also shown are $|C|$ distributions for the A and B modes of the *optimal* $\lambda_{k/3}$ disturbance. The roughness-induced disturbance is clearly not optimal. And, because the purely imaginary $\alpha$ increases with increasing $k$, it is clear that the roughness-induced disturbance will decay substantially faster than the optimal disturbance. *Figure 10 is the first rigorous quantification of the receptivity of transient growth to roughness and provides the first quantitative description of how roughness-induced disturbances are suboptimal.*

Of course, the $C(\alpha)$ data is only useful to the extent that it can accurately reconstruct the disturbance profiles and the downstream evolution of the disturbances. Figure 11 compares the DNS data for the $\lambda_{k/3}$ mode's wall-normal $\hat{U}$, $\hat{V}$ and $\widehat{W}$ profiles. The streamwise disturbance is reconstructed exceptionally well while the spanwise and wall-normal disturbances are reconstructed
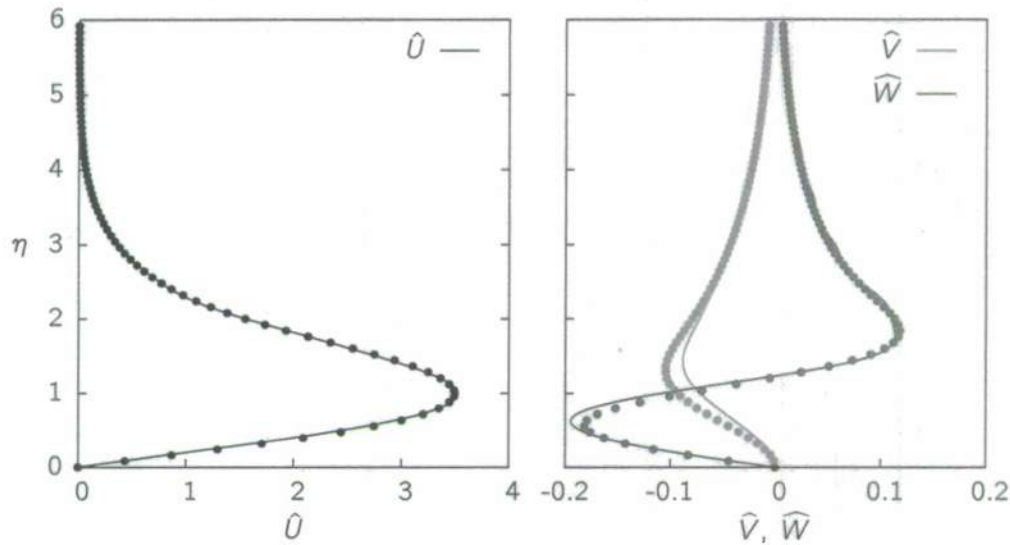
21

Figure 11: Comparison of $\lambda_k/3$ wall-normal disturbance component profiles generated by DNS (symbols) at $x = 325$ mm to profiles reconstructed from $C(\alpha)$ distributions generated by Eqn. 18 (lines).

with somewhat less accuracy. Because the comparison is made at the location from which the input data is drawn, these profiles should match exactly. The extent to which they do not indicates that the flow is not perfectly modeled by the OS Equation. Non-parallel effects, finite-amplitude disturbances and non-zero Reynolds stresses all might lead to the discrepancies between the DNS results and the reconstructed profiles. It should be noted that the discrepancies that do exist are about 0.5% of the maximum $\hat{U}$ disturbance, on the order of the non-parallel terms neglected from the OS equations, $Re_\delta^{-1}$. Some ripples are evident in the $\widehat{W}$ profile above $\eta = 2$. This may be an indication that a finer discretization of the continuous spectrum could produce improved results.

The ability of the biorthogonal decomposition to predict disturbance growth is shown in Fig. 12. This figure compares DNS results for the $\lambda_{k/3}$ disturbance at four locations to the energy evolution predicted by the decomposition performed at the most upstream of these points, $x = 325$ mm. Because the boundary layer thickness increases over the measurement domain, the streamwise position is made nondimensional by integrating $x$ from $x_k$ to a position of interest normalized by the local boundary layer thickness $\delta(x)$ as

$$\xi = \int_{x_k}^{x} \frac{dx}{\delta(x)}. \tag{30}$$

The biorthogonal decomposition is performed using a parallel-flow approximation and using $\xi$ only accounts for non-parallel effects in a crude way. Nevertheless, the ability of the biorthogonal decomposition to predict downstream energy growth is quite good for a distance exceeding $100\delta$. Also shown is the energy of the $\lambda_{k/3}$ mode streamwise disturbance energy measured by the experiment. Error bars represent 95% confidence intervals. The comparison makes clear that the experiment and DNS differ in some important respects but are in general qualitative agreement. Overall, the success of the biorthogonal decomposition to analyze DNS data even with relatively large steady disturbances is quite good.

The two attempts to decompose the experimental data were not as successful as the decomposition of the DNS data. The first attempt was to decompose using $\hat{U}$ and $\widehat{W}$ data. This resulted in reasonably
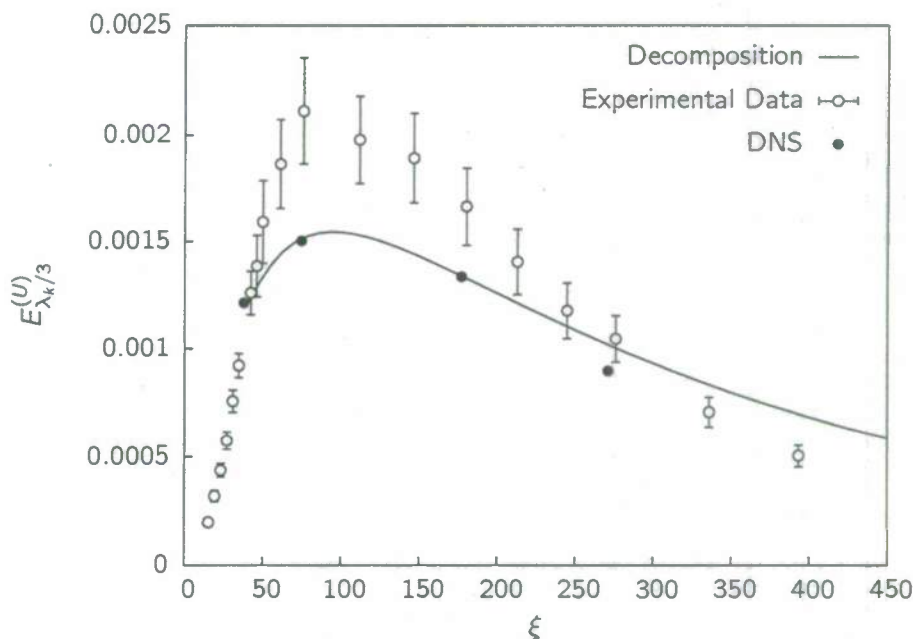
Figure 12: Comparison of streamwise-disturbance energy of the $\lambda_k/3$ disturbance mode of the DNS simulation, the biorthogonal decomposition of the simulation data and the experiment.

accurate $\hat{U}$ profiles but inaccurate $\widehat{W}$ profiles. This reinforces the notion that the $\widehat{W}$ data is incorrectly measured. It is expected that the disturbances are reasonably well modeled by the OS Equation. The DNS results reinforce this view. So, the fact that the modes of the OS Equation *cannot* reproduce the measured results indicates the measurements are not solutions of the OS Equation. And, as would be expected from a decomposition of incorrect data, the energy evolution predicted by the decomposition do not agree with either the experimental or DNS results.

Second, a decomposition was attempted using just $\hat{U}$ data. Although this data is thought to be accurate, the decomposition using this limited input data was not successful. The $\hat{U}$ profile was reproduced correctly but the energy evolution was not. Because the $\hat{V}$ and $\widehat{W}$ represent the initial condition of transient growth but no information about either of these disturbances was supplied to the decomposition procedure, it is not surprising that this effort did not succeed. It is clear that in performing decompositions with partial data, it is necessary that the input data include some information about the decaying streamwise vortex that initiates transient growth.

## 5   Conclusion

This one-year project, FA9550-07-1-0312, sought to complete the transient growth receptivity study begun as AFOSR Project FA9550-05-1-0048. The present work focused on the biorthogonal decomposition of measured disturbances behind a spanwise array of cylindrical roughness elements and a DNS study of the experiment.

Comparison of the experimental and DNS results proved quite useful as it revealed that the spanwise disturbances measured in the experiment to be incorrect. An extensive effort to reanalyze the experimental data using a Monte Carlo–based error propagation technique clearly establishes the dif-

ference between the experiment and DNS in terms of the spanwise disturbance velocities. The Monte Carlo technique is quite general and is an effective means of analyzing the uncertainty of experimental results when instrument calibration uncertainties lead to highly covariant uncertainties in the results.

Biorthogonal decomposition was performed on both experimental and DNS data. The effort was successful for the DNS data. Reconstructed disturbance profiles are in good agreement with the original data and the energy evolution predicted by the decomposition is in good agreement with the DNS results for an extensive streamwise extent. Most importantly, the results are the first to rigorously quantify transient growth receptivity and are the first to explicitly quantify the way in which roughness-induced disturbances differ from optimal disturbances.

The decomposition efforts were not successful using the experimental data. When incorrect spanwise disturbances were included in the calculation, these were not reproduced. This reconfirms that the data are erroneous. When only the streamwise disturbances were included there was insufficient information about the initial disturbance environment to correctly predict downstream behavior.

Overall, the goal of analyzing transient growth receptivity has been partially achieved. Efforts using the DNS data were successful and confirm important points about non-optimal disturbances. However, more work remains before experimentally measured disturbances can be analyzed in the same manner and with the same success. It is important that these efforts continue because DNS of surfaces with realistic distributed roughness will remain prohibitively difficulty for some time.

# References

Andersson, P., M. Berggren, and D. S. Henningson (1999). Optimal disturbances and bypass transition in boundary layers. *Phys. Fluids 11*(1), 134–150.

Bevington, P. R. (1969). *Data Reduction and Error Analysis for the Physical Sciences.* McGraw-Hill.

Bruun, H. H. (1995). *Hot-Wire Anemometry Principles and Signal Analysis.* Oxford University Press.

Butler, K. and B. Farrell (1992). Three-dimensional optimal perturbations in viscous shear flow. *Phys. Fluids A 4*(8), 1637–1650.

Denissen, N. A. and E. B. White (2008). Roughness-induced bypass transition, revisited. *AIAA J. 46*(7), 1874–1877.

Downs, Robert S., I. and E. B. White (2008). Transient growth and transition induced by random distributed roughness. *AIAA J. 46*(2), 451–462.

Ergin, F. G. and E. B. White (2005). Multicomponent and unsteady velocity measurements of transient disturbances. AIAA Paper 2005-0527.

Ergin, F. G. and E. B. White (2006). Unsteady and transitional flows behind roughness elements. *AIAA J. 44*(11), 2504–2514.

Farrell, B. F. (1988). Optimal excitation of perturbations in viscous shear flow. *Phys. Fluids 31*, 2093.

Gregory, N. and W. S. Walker (1956). The effect on transition of isolated surface excrescences in the boundary layer. Technical Report R. & M. 2779, Aero. Res. Council.

Hinze, J. O. (1959). *Turbulence. An introduction to its mechanism and theory.* New York: McGraw-Hill.

Jørgensen, F. E. (1971). Directional sensitivity of wire and fibre-film probes. *DISA Info. 11*, 31–37.

Kendall, J. (1981). Laminar boundary layer velocity distortion by surface roughness: Effect upon stability. AIAA Paper 81-0195.

Luchini, P. (2000). Reynolds-number-independent instability of the boundary layer over a flat surface: Optimal perturbations. *J. Fluid Mech. 404*, 289–309.

Press, W., S. Teukolsky, W. Vetterling, and B. Flannery (2001). *Numerical Recipes in C* (2nd ed.). Cambridge University Press.

Reshotko, E. (2001). Transient growth—A factor in bypass transition. *Phys. Fluids 13*(5), 1067–1075.

Reshotko, E. and L. Leventhal (1981). Preliminary experimental study of disturbances in a laminar boundary layer due to distributed roughness. AIAA Paper 81-1224.

Reshotko, E., W. S. Saric, and H. M. Nagib (1997). Flow quality issues for large wind tunnels. AIAA Paper 97-0225.

Rice, J. M. (2004). Roughness receptivity and scaling of non-optimal transient disturbances. Master's thesis, Case Western Reserve University.

Rizzetta, D. P. and M. R. Visbal (2007). Direct numerical simulations of flow past an array of distributed roughness elements. *AIAA J. 45*(8), 1967–1976.

Saric, W. (2007). Boundary-layer stability and transition. In C. Tropea, A. L. Yarin, and J. F. Foss (Eds.), *Springer Handbook of Experimental Fluids Mechanics*, pp. 886–896. Berlin: Springer.

Schmid, P. J. and D. S. Henningson (2001). *Stability and transition in shear flows*. New York: Springer.

Tani, I., A. Komoda, Y. Komatsu, and M. Iuchi (1962). Boundary layer transition by isolated roughness. Technical Report 375, Aero. Res. Inst., Tokyo Univ.

Tumin, A. (2003). Multimode decomposition of spatially growing perturbations in a two-dimensional boundary layer. *Phys. Fluids 15*(9), 2525–2540.

Tumin, A., M. Amitay, C. Jacob, and M. D. Zhou (1996). A normal multimode decomposition method for stability experiments. *Phys. Fluids 8*(10), 2777–2779.

Tumin, A. and E. Reshotko (2001). Spatial theory of optimal disturbances in boundary layers. *Phys. Fluids 13*(7), 2097–2104.

White, E. B. (2002). Transient growth of stationary disturbances in a flat plate boundary layer. *Phys. Fluids 14*(12), 4429–4439.

White, E. B. and F. G. Ergin (2003). Receptivity and transient growth of roughness-induced disturbances. AIAA Paper 2003-4243.

White, E. B., J. M. Rice, and F. G. Ergin (2005). Receptivity of stationary transient disturbances to surface roughness. *Phys. Fluids 17*(6), 064109.

Zhigulev, V. N. and A. Tumin (1987). *Origin of Turbulence*. Novosibirsk: Nauka. In Russian.